

6-2019


Effects of Pulse Width on He Plasma Jets in Contact with Water Evaluated by OH(A-X) Emission and OH_{aq} Production

Shutong Song
Old Dominion University

Esin B. Sözer
Old Dominion University

Chunqi Jiang
Old Dominion University, cjiang@odu.edu

Follow this and additional works at: https://digitalcommons.odu.edu/bioelectrics_pubs

 Part of the [Biomedical Commons](#), and the [Plasma and Beam Physics Commons](#)

Repository Citation

Song, Shutong; Sözer, Esin B.; and Jiang, Chunqi, "Effects of Pulse Width on He Plasma Jets in Contact with Water Evaluated by OH(A-X) Emission and OH_{aq} Production" (2019). *Bioelectrics Publications*. 273.
https://digitalcommons.odu.edu/bioelectrics_pubs/273

Original Publication Citation

Song, S. T., Sozer, E. B., & Jiang, C. Q. (2019). Effects of pulse width on he plasma jets in contact with water evaluated by oh(a-x) emission and OH_{aq} production. *Japanese Journal of Applied Physics*, 58(6), 066002. doi:10.7567/1347-4065/ab1e6d

REGULAR PAPER



Effects of pulse width on He plasma jets in contact with water evaluated by OH(A-X) emission and OH_{aq} production

To cite this article: Shutong Song *et al* 2019 *Jpn. J. Appl. Phys.* **58** 066002

View the [article online](#) for updates and enhancements.



Effects of pulse width on He plasma jets in contact with water evaluated by OH(A-X) emission and OH_{aq} production

Shutong Song^{1,2*} , Esin B. Sözer¹, and Chunqi Jiang^{1,2*} ¹Frank Reidy Research Center for Bioelectrics, Old Dominion University, Norfolk, VA 23529, United States of America²Department of Electrical and Computer Engineering, Old Dominion University, Norfolk, VA 23529, United States of America*E-mail: ssong003@odu.edu; cjiang@odu.edu

Received March 14, 2019; revised April 8, 2019; accepted April 30, 2019; published online May 22, 2019

Nanosecond pulsed helium plasma jets impinging on water produce hydroxyl radicals both in gas- and liquid-phase. In this study, the effects of pulse width on a repetitively pulsed plasma jet in contact with water are evaluated via OH(A-X) emission and OH_{aq} production in water for various pulse widths ranging from 200 to 5000 ns. The maximal energy efficiency of OH(A-X) emission is obtained for pulse widths of 600–800 ns whereas the maximal efficiency of OH_{aq} production is at 200 ns. Temporally-resolved emission spectroscopy shows that more than 40% of OH(A-X) emission is produced during the first 200 ns of the voltage pulse regardless of the pulse width. An equivalent circuit model of the plasma jet impinging on water is compiled to understand the charge transfer process, which is important for OH_{aq} production via charge exchange reactions.

© 2019 The Japan Society of Applied Physics

1. Introduction

The growing interests in plasma medicine^{1–4)} encourage studies of non-thermal, atmospheric pressure plasma jets interacting with water since the biological targets (cells or tissues) are either in aqueous solutions or covered by a thin layer of water.^{5–7)} Reactive oxygen and nitrogen species (RONS) produced in the plasma jets penetrate through the wet surface and induce further reactions, which affect cells and tissues in liquids.^{6,8,9)} Depending on the concentration of RONS on the biological target, this interaction could be beneficial or harmful since RONS are known to be able to influence many biological functions.⁸⁾ Among plasma-generated RONS, OH is of peculiar interest in many biomedical applications due to its high oxidative effect^{10–12)} and has been considered to play an important role in cell treatment.^{7,8)} Previous studies showed that the presence of water could highly affect the spatial and temporal distribution of OH in plasma plumes by comparing plasma jets in air with in contact with water.^{13,14)} Along the discharge gap between the jet nozzle and water surface, a bimodal distribution of OH emissions was observed with strong peaks near the jet nozzle and the water surface via spatially-resolved optical emission spectroscopy.¹⁴⁾ By using laser-induced fluorescence, it was found that a large amount of ground state OH formed a conical shape within 2 mm above the water surface with a maximal concentration of $1.7 \times 10^{14} \text{ cm}^{-3}$.¹³⁾ Computational studies showed that OH could be largely produced in the plasma column as well as near the water surface when a pulsed plasma jet was directed onto a water layer with 200 μm in thickness.⁹⁾ Interactions of a plasma jet with three different surfaces (i.e. the glass plate as dry surface, the rat surface and the wet surface formed by melamine sponge absorbing distilled water) revealed that OH reached the highest concentration of $2 \times 10^{13} \text{ cm}^{-3}$ with presence of wet surface.¹⁵⁾ Measurement of OH in liquid phase were carried out by many groups via a variety of methods including spin-trap and chemical probes for atmospheric pressure plasmas interacting with liquids.^{16–19)} For a pulsed streamer discharge on liquid surface, the production rate of liquid phase OH_{aq} was estimated to be in the order of 10^{-9} M s^{-1} using a chemical probe method in which terephthalic acid (TA) was

employed to trap aqueous OH_{aq} forming 2-hydroxyterephthalic acid (HTA).¹⁶⁾ Using electron spin resonance spectroscopy, the production rate of the DMPO (5,5-dimethyl-1-pyrroline-N-oxide) hydroxyl radical adduct was measured to be around 80 pmol s^{-1} , which equals to an OH concentration of $2.88 \mu\text{M}$ for an argon plasma jet interacting with 5 ml DMPO solution.¹⁰⁾ Computational studies revealed that the generation of aqueous OH in the solution after plasma treatment may be a result of several processes including charge exchange reactions by positive ions striking the water surface, photolysis and the solvation of gas phase OH.⁹⁾ Manipulation of OH concentration is hence of great importance to achieve a beneficial interaction between OH and the biological target.

Pulsed atmospheric pressure plasmas have been studied intensively not only because of their relatively higher energy efficiency in producing some reactive species compared to discharges driven by kilohertz AC and RF sources^{20,21)} but also due to their flexible pulse parameters (i.e. amplitude, repetition rate, rise time and pulse width). Among many of the pulse parameters, pulse width was found to play a complex role in producing reactive species in both gas- and liquid-phase.^{22–24)} It was reported that OH concentration in liquid increased with treatment time¹⁶⁾ or pulse amplitude²⁵⁾ keeping the other pulse power parameters (e.g. the pulse width) constant. The dependence of the production of reactive plasma species on pulse width, however, was found not consistent. In a recent study of the effects of pulse width on microsecond-pulsed helium plasma jets for reactive species production and DNA damage, the OH_{aq} production was found decreasing with pulse width increasing from 2 to 10 μs .²²⁾ Emission intensities from several excited species including OH(A) and O($3p^5P$) remained constant for the three pulse widths tested, i.e. 2, 5 and 10 μs .²²⁾ However, these studies were all based on the use of voltage pulses with 2 μs and longer durations. Compared to previous reported studies related to plasma jets and analysis using emission spectroscopy or chemical probes, where the pulse widths were in microseconds range,^{22,26,27)} systematic studies of the pulse width effects on atmospheric pressure nanosecond pulsed plasma jets (APNPs), powered by voltage pulses with nanosecond pulse widths (e.g. $< 500 \text{ ns}$) are rare.

In this study, the correlation between the nanosecond pulse width (in the range of 200–5000 ns) and the OH(A–X) emission using spatiotemporally-resolved optical emission spectroscopy, where the contribution of different discharge phases to the emission intensities are discussed. The dependence of the liquid phase OH concentration in water on the pulse width are investigated using a chemical probe method. Importantly, an equivalent circuit model is compiled based on the voltage and current measurements of the plasma jets to elucidate the importance of charge exchange reactions for the OH_{aq} production.

2. Experimental methods

Schematic of the experimental setup for optical emission spectroscopy and electrical measurements is shown in Fig. 1. A plasma jet device, consisting of a hollow-needle electrode and water in a grounded container, generated a plasma plume between the needle nozzle and water surface when it was powered by 6 kV pulses at 1 kHz and with a helium flow. The hollow-needle was made of stainless steel with the inner and outer diameters being 0.254 mm and 0.508 mm, respectively. A nanosecond high voltage (HV) pulse generator (DEI PVX-4110) was used for this study. The ultra-high purity helium (99.999% minimum purity) was used as the feed gas and regulated by a mass flow controller (MKS Instruments 146C) at a flow rate of 70 sccm (standard cubic cm per min) throughout the experiments. The flow velocity was calculated to be 23 m s⁻¹ with Reynolds number 49, which indicates a laminar flow. The custom-built water container consists of a conductive bottom made of a 75 × 25 mm² copper plate with thickness of 1 mm and four fused silica glass walls of the same height of 25 mm, hence forming a rectangular cuboid with a dimension of 75 × 25 × 25 mm³. The conductive bottom was grounded to the transmission line ground. Ultra-high purity water (relative permittivity = 80, resistivity = 18.2 MΩ cm) was used to fill the container. The needle electrode was placed perpendicular above the water surface at a nozzle-to-surface distance of $d = 10$ mm. For this gap distance, a dent was observed at the water surface because of the helium gas flow.¹⁴ The applied voltage and total current were measured at the load end of the transmission line using a HV probe (Tektronix 6015 A) and a current monitor (Pearson 6585), respectively. Another

current monitor (Pearson 6585) was placed at the discharge gap for measurement of the jet current as shown in Fig. 1.

Optical emission spectroscopy was employed to detect emissions from OH (A–X). A 0.75 m Czerny–Turner spectrograph (Princeton instruments, model SP2750) coupled with an ICCD camera (Princeton Instrument PI-MAX 4) was used for spectral analysis. The ICCD has a 1024 × 1024 pixel array with a single pixel size of 12.8 μm × 12.8 μm. The plasma plume produced between the jet nozzle and water surface was focused by the UV enhanced two-mirror system (a plano and a concave mirrors) with a focal length of 75 mm for the concave mirror and was displayed on the slit with a 1:1 magnification forming a spatial resolution of ~50 μm. A holographic grating which has a groove density of 1800 g mm⁻¹ was used for spectral dispersion. The slit width was set to 20 μm. The spectral resolution was about 0.02 nm. The OH (A–X) spectrum from 306 nm to 312 nm was accumulated over 8000 shots. The spatially-integrated OH spectrum was obtained by integrating the OH spectrum over the axial distance between the jet nozzle to the water. To investigate the total temporally-resolved OH (A–X) emission, a bandpass filter (center wavelength 309 nm, full width half maximum (FWHM) 10 nm) was used to replace the spectrometer and inserted between a UV–visible fused silica bi-convex lens (focal length = 75 mm) and the ICCD camera. The ICCD exposure time was fixed at 5 ns with accumulation of 20 000 pulses for each measurement. For both optical emission spectroscopy and ICCD imaging, the ICCD camera and the pulsed power supply were synchronized using a function generator (BNC, Model 745).

To access the potential effect of heating in water and the vicinity above the water surface where plasma impinging on water for OH(A–X) emission and OH_{aq} production, the gas temperature of the APNPJ in the region 1 mm above the water surface was measured by comparing the recorded OH (A–X) emission with simulated (Specair[®]) emission lines. In addition, a fiber optic temperature sensor (Neoptix, T1S-2M) was placed directly in the plasma plume at 1 mm above the water surface to assess the gas temperature or right below the water surface to measure the water temperature for various pulse widths.

In order to detect OH_{aq} in liquid phase, TA was used as a scavenger molecule. Using terephthalic acid (TA) for OH_{aq} detection is an established method with advantages over common fluorescent methods that are used for ROS detection.^{28,29} TA is a non-fluorescent molecule, which specifically reacts with OH radical resulting in the stable and fluorescent molecule 2-hydroxyterephthalic acid (HTA).^{16,30,31} As shown in Fig. 2(a), a small centrifuge tube with a volume of 1.5 ml, containing 0.5 ml of 0.2 mM TA solution (diluted from stock solution with 2 mM TA and 14 mM NaOH), was used to replace the water electrode to ensure a detectable HTA in the liquid after the plasma treatment. The tube was inserted into a grounded copper holder at its bottom. The TA solutions were treated with He flow of 70 sccm (plasma off) for 5 min as the negative control group, or with the plasma plume at 6 kV, 1 kHz at various pulse widths for the same time as the plasma treatment. The distance from needle nozzle to liquid surface was constant at 10 mm. For each experimental condition, total of six samples were treated 2 samples per day in three different days. After

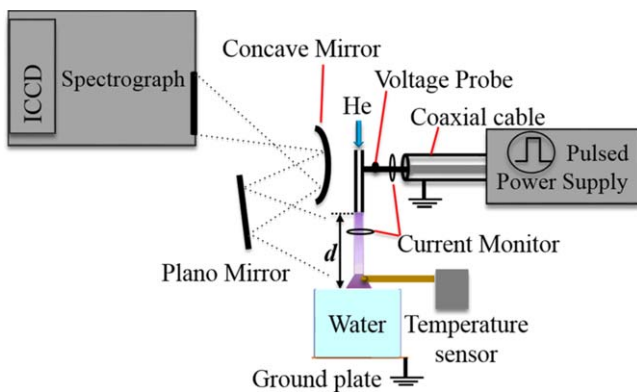


Fig. 1. (Color online) Schematic of optical emission spectroscopy and electrical measurement of a plasma jet impinging on a water electrode. The discharge gap distance d , from jet nozzle to liquid surface, is 10 mm.

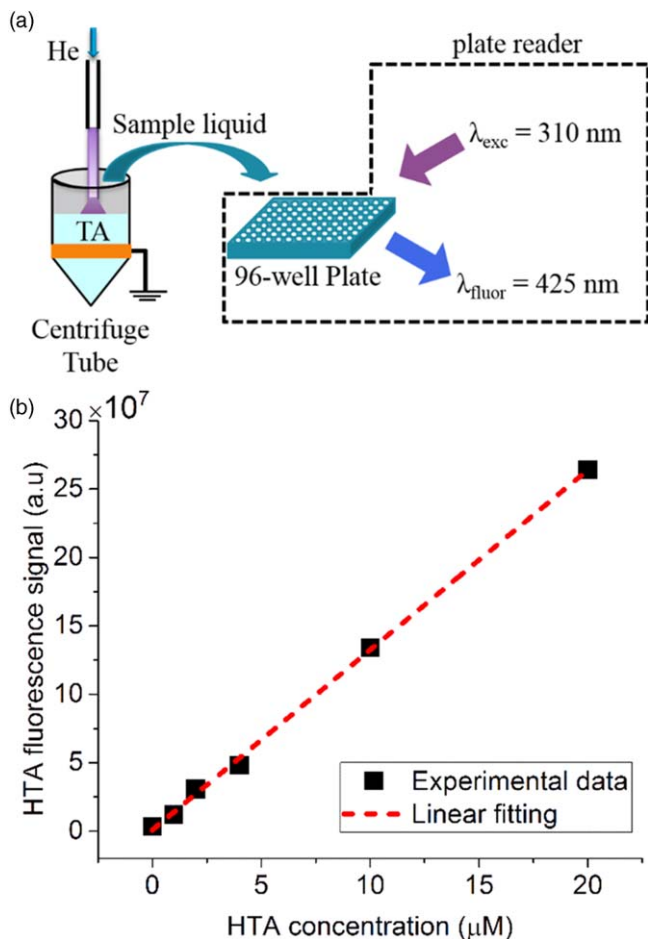


Fig. 2. (Color online) (a) Schematic of the terephthalic acid (TA)-based measurement of aqueous OH concentration in water after the treatment with the plasma jet powered by 6 kV pulses with various pulse widths. During the treatment, the gap distance between the HV electrode nozzle and the liquid surface of the TA solution is 10 mm and the plasma exposure time is 5 min (b) HTA concentration calibration based on HTA fluorescence measurements: comparison of the experimental data (black dot) and linear fitting (red dash line) with respect to the known HTA concentration.

transferring 300 μl of the solutions from each centrifuge tube to 3 different wells ($3 \times 100 \mu\text{l}$) of 96-well plates, HTA fluorescence was measured with excitation wavelength $\lambda_{exc} = 310 \text{ nm}$ and emission wavelength of $\lambda_{fluor} = 425 \text{ nm}$ using a plate reader (Molecular Devices SpectraMax i3). The measured fluorescence was calibrated to HTA concentration following a pre-calibration procedure where HTA solutions of known concentrations were prepared and measured under same fluorescence measurement conditions [shown in Fig. 2(b)].³¹⁾ The reaction from TA to HTA has a 35% which was used to estimate final OH concentration in liquid accumulated during the treatment.³¹⁾

3. Results

3.1. Voltage–current, energy per pulse and gas temperature

The voltage and current of the helium plasma jet with water electrode at a pulse repetition rate of 1 kHz for various pulse widths (t_{pw}), ranging from $t_{pw} = 200$ to 5000 ns, are shown as in Fig. 3(a). The voltage amplitude was kept the same at 6.0 kV. The shortest pulse has a FWHM of 164 ns [the black solid line in Fig. 3(a)]. For convenience, the pulse width was

noted as $t_{pw} = 200 \text{ ns}$. For longer pulse widths, the pulse width was noted similarly and the corresponding FWHM was 36 ns less than the named t_{pw} or $\text{FWHM} = t_{pw} - 36 \text{ ns}$. The current, shown by a dash-dot line, is displayed in the same color as the corresponding voltage pulse. It was measured by placing the current monitor at one end of the transmission line close to the plasma (shown in Fig. 1) with plasma on and included both displacement and conduction currents. Total energy consumption is evaluated using this current with voltage measured at the same location. It indicates the total energy consumed by the load. The positive and negative current peaks during the rising and falling phases of the voltage pulse showed strong dependence of the current on dV/dt , which is typical for a dielectric barrier discharge.

The energy per pulse was calculated by integrating the product of discharge voltage and current over a sufficient period of time that includes complete voltage and current pulses and post-discharge ringing. Three repeated measurements were conducted for each pulse width. The averaged energy per pulse of the APNPJ with different pulse widths and its linear fitting ranging from 200 to 5000 ns are shown in Fig. 3(b). The error bars in the figure correspond to the standard deviation from the average value at the pulse width condition. The energy deposited in the plasma increased with pulse width monotonically; the energy per pulse was measured to be 397 μJ for $t_{pw} = 5000 \text{ ns}$, which is 1.7 times as that for $t_{pw} = 200 \text{ ns}$.

Although the energy deposited in the plasma and the change in energy with pulse width are relatively small, the potential heating effect due to pulse width increasing was investigated by measuring the gas temperature of the APNPJ just above the water surface and the water temperature just below the plasma–water intersection. Figure 4(a) showed the time-averaged emission spectra of OH (A–X) of the APNPJ powered by 6 kV pulses at 1 kHz for a range of pulse width, comparing with the simulated (Specair®) emission lines at a rotational and vibrational temperature of $310 \pm 30 \text{ K}$ and $3500 \pm 30 \text{ K}$, respectively. The well-overlapped emission lines for different pulse widths show that variation in the gas temperature over the range of investigated pulse width, from 200 to 5000 ns, is negligible, and the gas temperature of the APNPJ at that location can be considered to be near the room temperature. It is hence feasible to use the fiber optic temperature sensor to measure the gas temperature of the APNPJ by inserting the probe of the temperature sensor directly into the APNPJ and 1 mm above the water surface (as shown in Fig. 1). Three repeats for each measurement were carried out. The mean gas temperature in the APNPJ was found about 295 K, with the maximum error of 8%, as shown in Fig. 4(b). In addition, the water temperature in the immediate vicinity of the water-hugging plasma and right below the water surface was measured to be 292.5 K with an estimated error of 3%, also as shown in Fig. 4(b). Both the fluctuations in temperature with respect to the pulse width are small and the temperature can be considered constant for the investigated pulse widths.

To better understand the discharge dynamic of the plasma jet, the jet current was evaluated by placing another current monitor at the discharge gap between the jet nozzle and the water surface (as shown in Fig. 1). The jet current, obtained

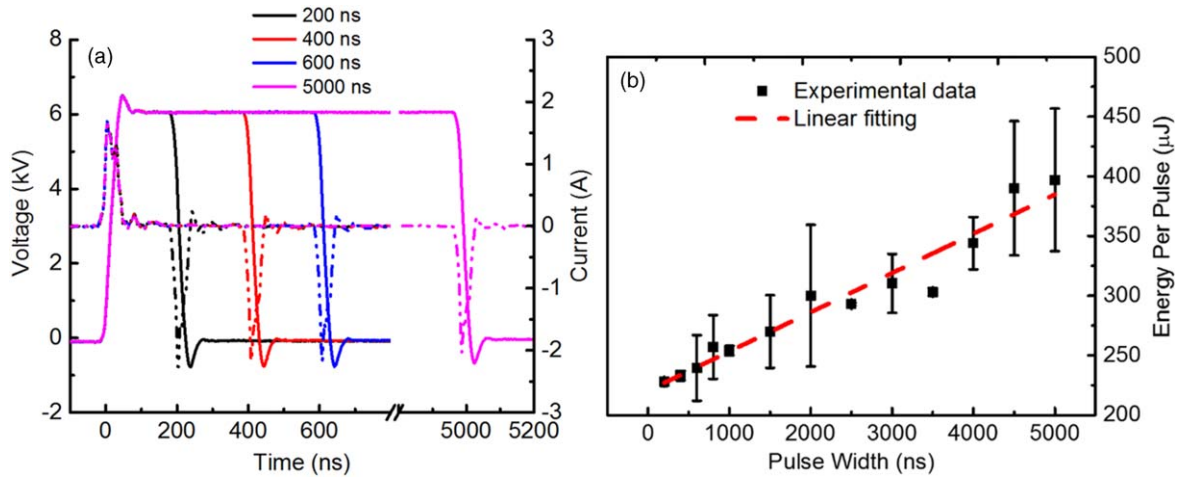


Fig. 3. (Color online) (a) Voltage (solid lines) and current (dash-dot lines) waveforms of the APNPJ operated at 1 kHz with various pulse widths (t_{pw} : 200, 400, 600 and 5000 ns); The current was indicated in the same color as the corresponding voltage. (b) Energy per pulse of the APNPJ with respect to the pulse width.

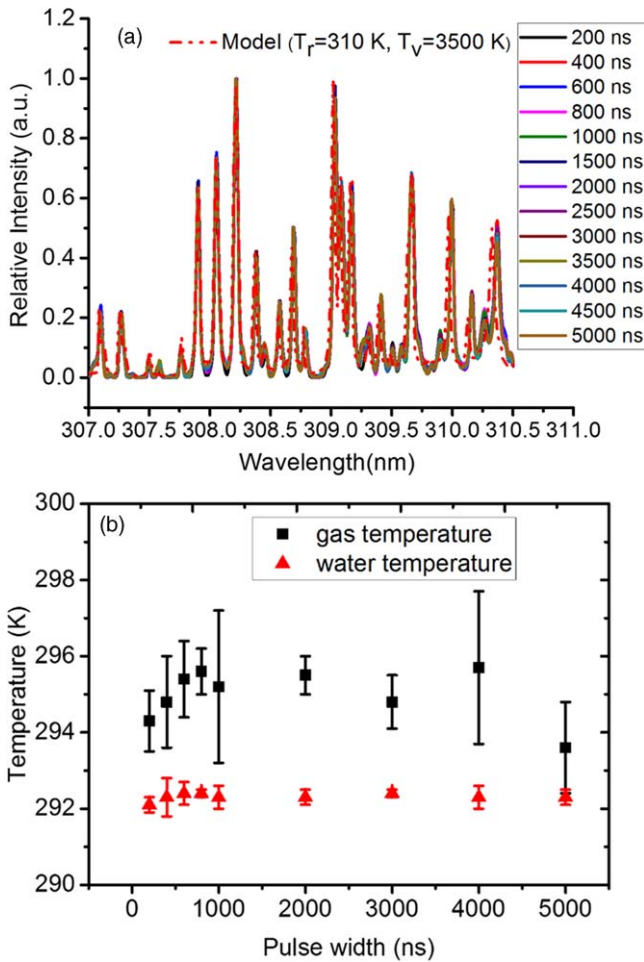


Fig. 4. (Color online) (a) Experimental (solid lines) and fitting (dot line) emission spectra of the OH(A-X) band to determine the rotational temperature of the APNPJ powered by 6 kV pulses at 1 kHz with pulse widths ranging from 200 to 5000 ns; (b) gas temperature of the APNPJ at 1 mm above the water surface (black rectangle) and the water temperature (red triangle) in the vicinity of the APNPJ and just below the water surface, recorded by the fiber optic temperature sensor, with respect to the pulse width.

by subtracting the assumed displacement current measured without He flow at the same pulsed voltage from that with He flow and hence the plasma was on, which is a good

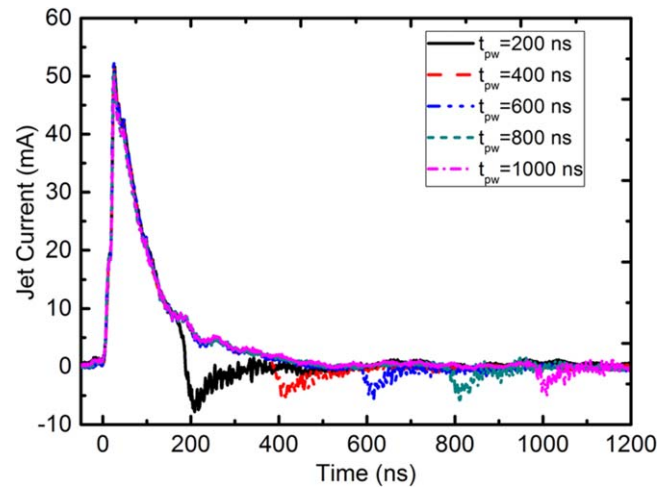


Fig. 5. (Color online) Jet currents of the APNPJs powered by 6 kV at 1 kHz voltage pulses with various pulse widths.

representation of the discharge dynamics of the plasma plume.¹⁴⁾ Figure 5 shown the jet currents for APNPJs driven by various pulse widths ranging from $t_{pw} = 200$ to 1000 ns. The positive and negative peaks in the jet current are associated with the discharges during the rising and falling phases of the voltage pulse, which are considered as the primary and secondary discharges, respectively.¹⁴⁾ The positive peaks of the jet currents for various pulse widths are the same at 52 mA. They are at least 10 times more than their correspondent negative peaks that occurred during the falling phase of the voltage pulses.

3.2. Total emission intensity of OH(A-X) versus the pulse width

The total OH (A-X) emission in gas phase was calculated by integrating the spectrum from 306 to 312 nm, followed by applying the spatial integration along the axial distance from the jet nozzle exit to the water surface. As shown in Fig. 6, the total integrated OH emission intensity increases to the maximum value with t_{pw} increasing from 200 to 800 ns. Further increasing t_{pw} resulted in a slight decrease in the OH emission; 77% of the maximum was measured at $t_{pw} = 5000$ ns. The relative energy efficiency of OH(A-X) emissions can be evaluated using the following Eq. (1):

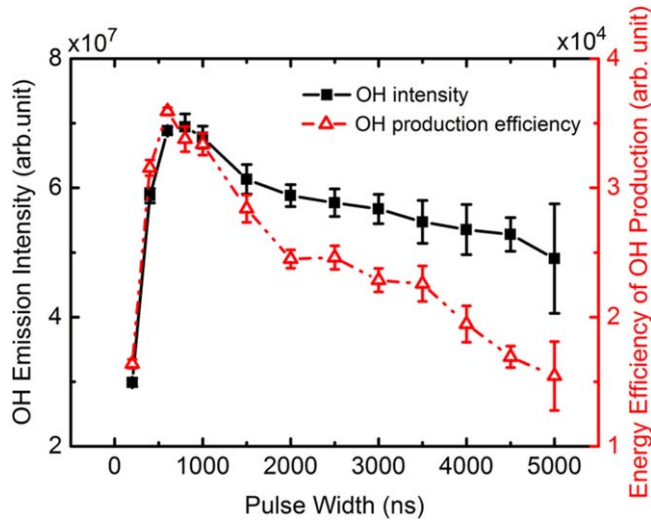


Fig. 6. (Color online) Total integrated OH intensity in gas phase (black square line) and its correspondent energy efficiency of OH(A–X) emissions (red triangle line) of the APNPJs powered by 6 kV, 1 kHz voltage pulses with pulse widths ranging from $t_{pw} = 200$ to 5000 ns.

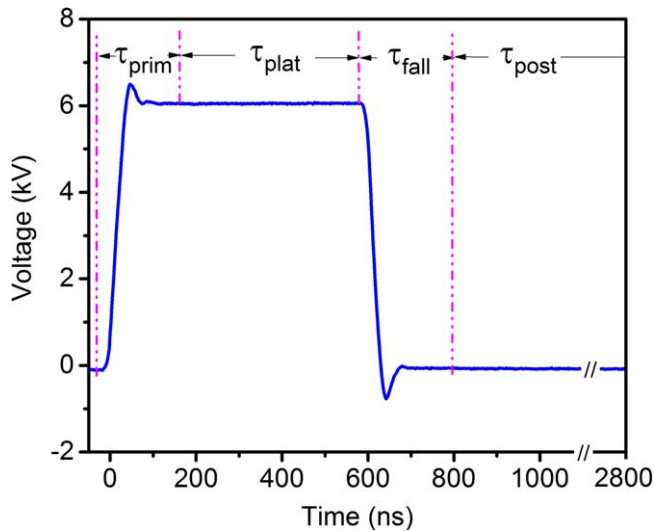


Fig. 7. (Color online) Four-phase segmentation of a 600 ns pulse width voltage pulse.

$$\text{Eff}_{\text{OH(A)}} = P_{\text{OH}} / (E_p \times N_p), \quad (1)$$

where P_{OH} is the total OH (A–X) emission intensity (arb. unit), E_p and N_p are the energy per pulse (Joule) and number of pulses accumulated (8000 pulses), respectively. The maximal energy efficiency was obtained in the APNPJs with 600 ns pulse width, as shown in Fig. 6.

3.3. Voltage-current, energy per pulse and gas temperature

In a pulsed plasma, the temporal variation of the voltage pulse impacts the discharge development. To understand the OH(A–X) emissions due to the temporal variation in the voltage pulse, we divided a voltage pulse into four phases: the primary phase, the plateau phase, the falling phase and the post-decay phase, as shown in Fig. 7. The primary phase, τ_{prim} , was defined as the first 200 ns from the onset of the voltage pulse. The plateau phase (τ_{plat}) is the additional plateau duration after the primary phase, and for $t_{pw} = 200$ ns, $\tau_{\text{plat}} = 0$. For longer pulses, the plateau phase

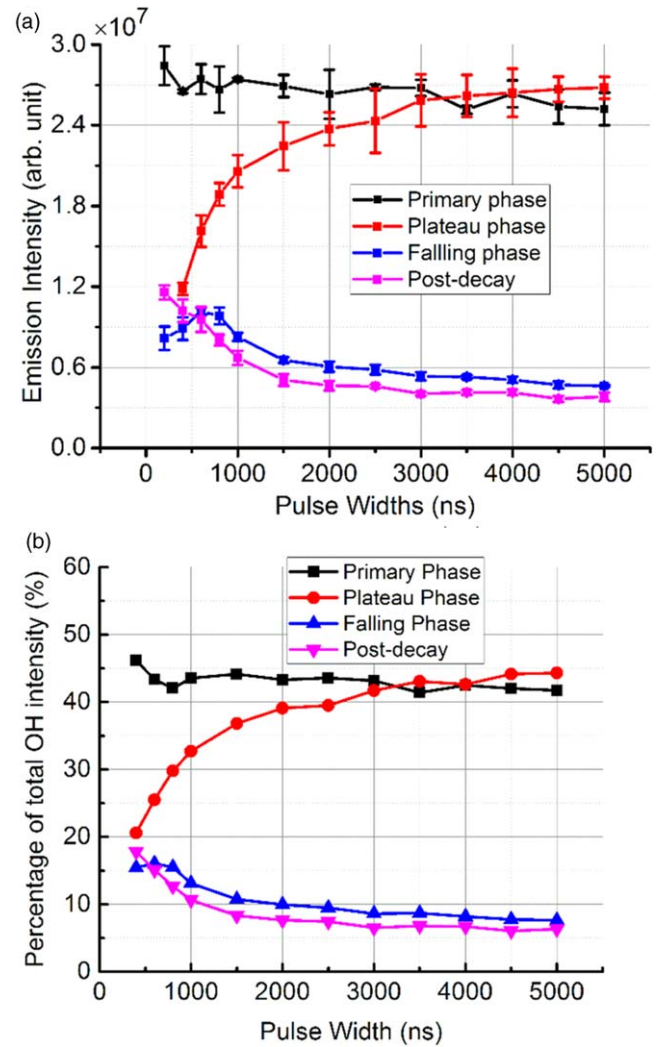


Fig. 8. (Color online) (a) OH(A–X) emission intensities generated in four phases with respect to the pulse width ranging from 200 to 5000 ns and (b) percentage of OH(A–X) emissions regarding its total intensity in four phases with respect to the pulse width ranging from 400 to 5000 ns.

becomes $\tau_{\text{plat}} = t_{pw} - 200$ ns (e.g. $\tau_{\text{plat}} = 400$ ns for $t_{pw} = 600$ ns). The falling phase (τ_{fall}) is constant for all the pulse widths and has a duration of 200 ns, which follows right after the plateau phase. The post-decay (τ_{post}) has a duration of 2 μs , which starts right after the falling phase. Figure 8(a) shows the OH emission during different voltage phases for various pulse widths. Contribution of OH(A–X) emission intensity in each voltage phase to the total intensity in percentage for $t_{pw} = 400$ to 5000 ns is shown in Fig. 8(b). It is found that a majority (or > 40%) of OH(A–X) emission is generated during the primary phases and the OH emission intensity remains about the same regardless of the pulse width. During the plateau phases, OH emission intensity increases by a factor of 2.3 as the pulse widths increases from 400 to 5000 ns [Fig. 8(a)]. Its contribution to the total OH emission intensity in percentage is accordingly increased from 20% to 43% with the pulse width increasing [Fig. 8(b)]. The OH emission intensity during the falling phase is small, less than 30% of that generated in the primary phase. The maximal intensity in the falling phase is observed for $t_{pw} = 600$ ns, and the percentage in the total OH emission intensity is $\sim 15\%$. During the post-decay, the

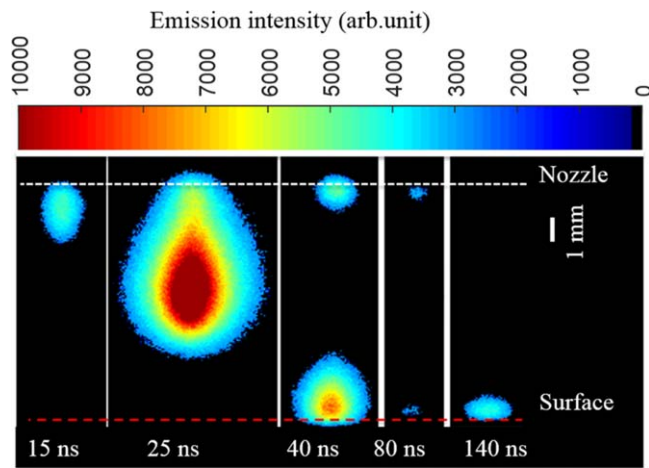


Fig. 9. (Color online) Spatiotemporal evolution of OH(A–X) emissions during the primary phase for $t_{pw} = 200$ ns. The white- and red- dash lines represent the jet nozzle and water surface, respectively. The time delay labeled in bottom of each image corresponds to the time in Fig. 3(a) and the exposure time of each image is 5 ns (same for Fig. 10).

OH intensity decreases monotonically with pulse width increasing.

Figures 9 and 10 show the images of the spatiotemporal evolution of OH from $t_{pw} = 200$ to 1000 ns using bandpass-filtered high speed imaging. The time delay, t_{delay} , (labeled on each image in the figures) corresponds to the time in Fig. 3(a). The spatiotemporally-resolved images of OH(A–X) emission from $t_{delay} = 15$ to 140 ns are the same for different pulse widths ranging from $t_{pw} = 200$ to 1000 ns, as shown in Fig. 9. This is also true for pulse widths up to $t_{pw} = 5000$ ns. The evolution of the OH(A–X) emissions after $t_{delay} = 160$ ns for various pulse widths was shown in Fig. 10. The evolution OH(A–X) emissions are similar during the primary phase (from $t_{delay} = 0$ to 180 ns) for different pulse widths due to the same discharge formation (the primary discharge) developed during the rising edge of the voltage pulse. The emission images during the falling phase of voltage pulse, however, varies significantly for pulse widths, particularly $t_{pw} \geq 200$ ns. If the pulse width is relatively short (e.g. $t_{pw} = 200$ ns), the conduction channel formed between the electrode and the water surface reduces the electric field around the nozzle anode and the secondary discharge during the voltage falling phase cannot form or is relatively weak. This is the case for $t_{pw} = 200$ –400 ns. With the application of longer (e.g. > 600 ns) pulse durations, the conduction channel formed between the electrodes was depleted and a stronger secondary discharge can form due to the higher field potential developed near the nozzle electrode during the falling phase of voltage pulse.

3.4. Dependence of OH_{aq} production on pulse width

Figure 11(a) shows the OH_{aq} concentration in water measured after 5 min of plasma treatment driven by varying pulse widths, $t_{pw} = 200, 500, 800, 1000, 2500$ and 5000 ns. Results were obtained from measurements of 6 repetitions for each pulse width. No OH_{aq} was detected for the negative control, where samples were exposed to only He flow and the plasma was turned off. For the plasma-treated samples, significant concentrations of OH_{aq} was measured, and its concentration in water was around $\sim 9 \mu\text{M}$, independent of the pulse widths. Figure 11(b) shows the energy efficiency of OH_{aq}

production by the ANPNJ, and was calculated using Eq. (1) with P_{OH} and E_p being the OH_{aq} concentration (μM) and energy per pulse (Joule), respectively. N_p is the total number of pulses applied for the treatment, and $N_p = 3 \times 10^5$. The maximal energy efficiency of OH_{aq} was measured to be $4.7 \times 10^{-5} \mu\text{M J}^{-1}$ at the shortest pulse width, $t_{pw} = 200$ ns.

4. Discussion

It is interesting to see that the highest OH(A–X) emission occurred for $t_{pw} = 600$ –800 ns. The phase dependence study showed that the majority of the emission intensity of OH(A–X) was produced during the primary phase of the pulsed voltage. However, the difference in emission intensities of OH(A–X) by voltage pulses with various widths was attributed to the voltage falling phase. In addition, the OH(A–X) emission generated during the falling phase was mostly near the HV needle electrode. An equivalent circuit model is hence presented here to elucidate the pulse width-dependence on the emission intensity of OH(A–X).

During the rising time of the voltage pulse, the jet current (Fig. 4) rises to its maximum (e.g. 52 mA) as a conduction channel forms between the needle nozzle and the water surface.¹⁴ Positive charges brought by the streamer head will accumulate at the water surface as if charging a capacitor. Hence a resistor R that represents the resistance of the conduction channel after streamer reached the water surface and a capacitor C that approximates the water electrode with negligible conductivity can be used as a time-dependent equivalent circuit for this system, and R and C are in series.

A RC constant ($\tau = RC$) can be estimated by fitting the decay of the positive jet current from its maximum using the following:

$$I(t) = I_0 e^{-t/\tau}, \quad (2)$$

where I_0 is 0.052 A (the maximal jet current) at $t = 0$. As shown in Fig. 12, the RC constant τ was calculated to be 116 ns. The water capacitor can be considered to be fully charged after 5 times the RC constant (5τ), which corresponds to a duration of ~ 580 ns. This agrees well with the experimental finding of the optimal pulse width, $t_{pw} = 600$ ns, for OH(A–X) emissions. It suggests that the amount of the surface charge transferred to the water surface is important to the secondary discharge, which occurs during the falling phase of the voltage pulse. The conduction channel is eventually consumed and the amplitude of the inverse of voltage potential near the needle electrode is proportional to the surface charge at the water surface. The voltage pulse hence has to be sufficiently long to allow the water electrode (as a capacitor) to be fully charged. The more the surface charge, the stronger the OH(A–X) emission during the secondary discharge. On the other hand, if the voltage pulse is relatively long, e.g. longer than 800 ns, the time interval between 5τ (being fully charged) and the falling phase would allow the loss of the surface charge due to diffusion and recombination to increase. This explains the reduced total OH(A) emission intensity for longer voltage pulse widths ($t_{pw} > 800$ ns) when compared with that for $t_{pw} = 600$ –800 ns.

In addition, using this RC model, the impedance of the APNPJ with water electrode system can be estimated. As shown in Fig. 3(b), the energy per pulse is linearly dependent

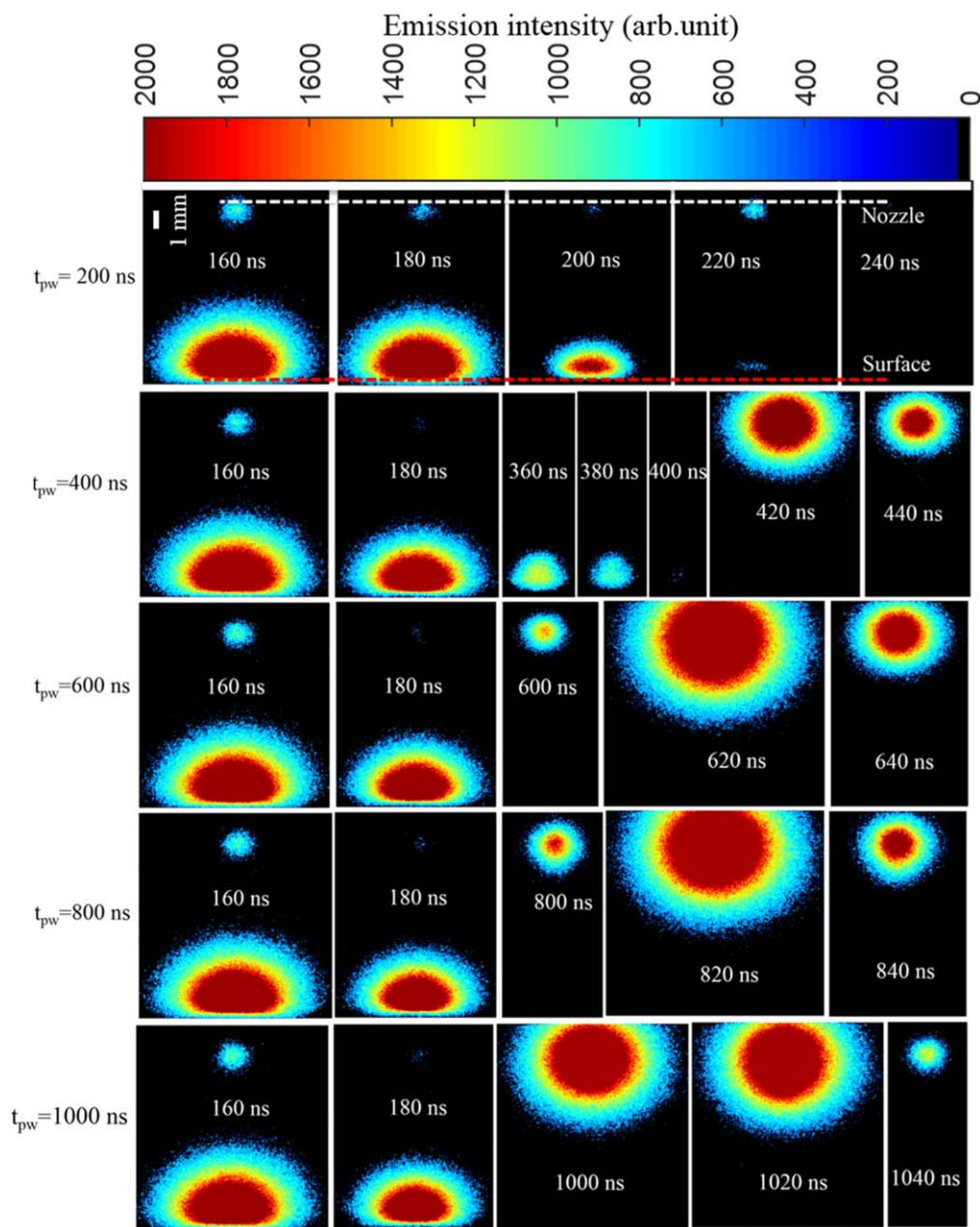


Fig. 10. (Color online) Continued spatiotemporal evolution of OH(A–X) emissions following Fig. 9 during the plateau and falling phases of voltage pulses for $t_{pw} = 200$ –1000 ns (time delay was labeled in middle of each image).

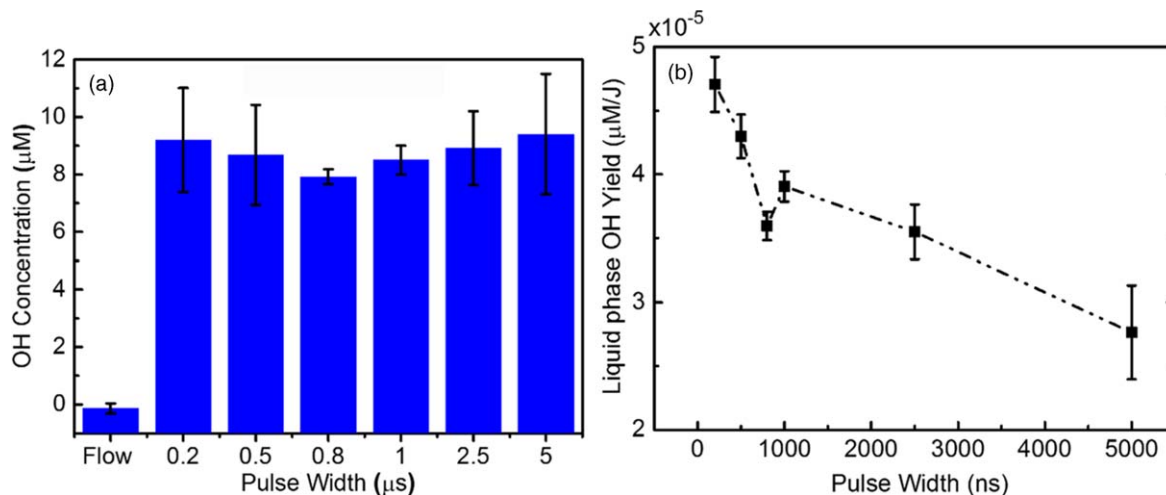


Fig. 11. (Color online) (a) OH_{aq} concentration in water after 5 min treatment by helium flow or the APNPJ powered by 6 kV, 1 kHz voltage pulses with various pulse widths ranging from $t_{pw} = 200$ to 5000 ns; and (b) the corresponding energy efficiency of OH_{aq} production by the APNPJs.

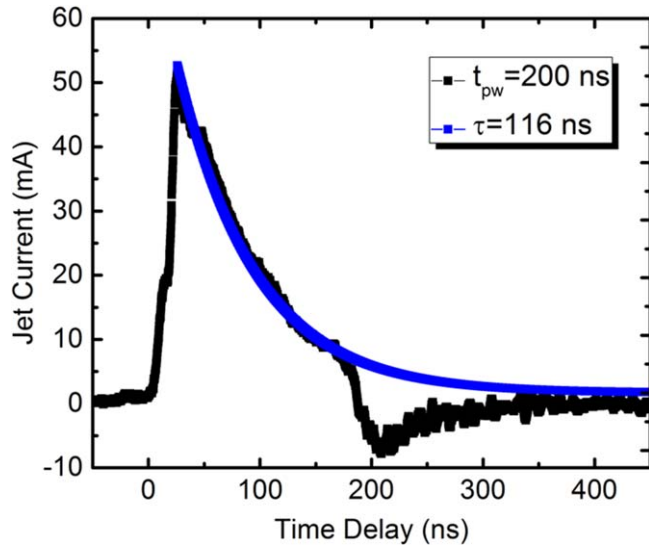


Fig. 12. (Color online) Fitting of the jet current ($t_{pw} = 200$ ns) using Eq. (2) from the equivalent RC circuitry.

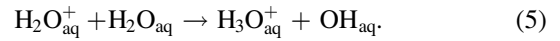
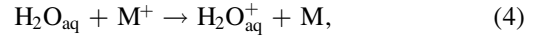
on the pulse width. If a rectangular pulse shape is assumed to all the voltage pulses, the energy per pulse E can be approximated by the following Eq. (3):

$$E = \frac{V^2 t_{pw}}{R} + E_{conn}, \quad (3)$$

where E_{conn} is the energy consumed by the connectors and electrodes without plasma, V is the voltage amplitude ($V = 6000$ V), t_{pw} is the pulse width, and R is the equivalent resistance of the plasma column. As shown in Fig. 3(b), the linear fitting to the energy per pulse as a function of the pulse width confirms that the plasma resistance R is constant for the studied pulse widths. At $t_{pw} = 0$, the energy consumed by the connectors and electrodes yields $E_{conn} = 220 \mu\text{J}$. The resistance of the plasma column R can be obtained and $R = 1\text{M}\Omega$. From Eq. (2), we have $\tau = RC = 116$ ns. The equivalent capacitance of the water capacitor can be estimated to be 0.12 pF. If we use a parallel-plate model to approximate the water capacitor, we then have the capacitance $C = \epsilon_r \epsilon_0 A/d$, where the absolute dielectric permittivity $\epsilon_0 = 8.85 \times 10^{-12}$ (F m^{-1}) and the relative permittivity $\epsilon_r = 80$ for water, and $d = 2.5$ cm as the depth of water or the distance between the water surface and the ground electrode. The effective area A , determined by the streamer plume impinging on the water surface, can be determined, and $A = C \cdot \frac{d}{\epsilon_0 \epsilon_r} = 3.8 \text{ mm}^2$. This results in a plume diameter of 2.2 mm on the water surface, which falls on the same order of magnitude of the observed diameter range of the emission intensity of the plasma jet impinging on water, as shown in Fig. 10.

Because the OH(A–X) emission involves the complete current pulse duration and the discharging process of the surface charge affects the secondary discharge at the needle electrode, the maximal total OH(A–X) emission was observed around 600 ns due to the pulse width-dependence of the secondary discharge. On the other hand, both the spatiotemporally-resolved OH(A–X) emissions and jet current measurements of the APNPJ with various pulse widths suggest the charge transfer from the plasma to the water surface only

occurs during the primary phase of the voltage pulse. The surface charge accumulated at the water surface has reached its maxima at the peak of the jet current. This implies that OH_{aq} production should be independent of pulse width if the OH_{aq} formation is dominated by charge exchange reactions such as those between positive charges M^+ (e.g. He^+ and He_2^+) and water molecules [Reactions (3)–(4)]:⁹⁾



Note that the pulse width-independence of OH_{aq} formation is on the condition that the shortest pulse width of the voltage is still sufficient to reach the maximal charge accumulation on the water surface. In addition, photolysis and diffusion of gas phase OH may also contribute to the OH_{aq} production but may play less significant roles. Photolysis typically requires VUV emission (wavelength < 200 nm) from highly excited states such as $\text{N}_2(\text{b}^1\Pi_u)$ and contributes only up to 10% of the total OH_{aq} production.⁹⁾ In this work, emission below 300 nm was not detected due to the significant quenching of short wavelength emissions at the atmospheric pressure. In addition, diffusion of gas phase OH into the liquid may also not be significant due to the quenching by heavy particles to form H_2O , H_2O_2 , etc.^{32,33)}

5. Conclusions

An atmospheric pressure pulsed He plasma jet in contact with water driven by 6 kV, 1 kHz under various pulse widths in the range of 200 to 5000 ns has been investigated for production of OH(A–X) emission and OH_{aq} . The maximal emission intensity of OH(A–X) occurred at pulse widths of 600 – 800 ns, whereas the production of OH_{aq} did not depend on the pulse widths. The maximal production efficiency of OH_{aq} was obtained for the shortest pulse width. The spatiotemporally-resolved optical emission spectroscopic study showed that the majority of the OH(A–X) emissions was produced during the primary phase (the first 200 ns) of the voltage pulse. A RC circuit model of the plasma showed that the surface charge on the water electrode impact on the secondary discharge and hence on the OH(A–X) emissions. In addition, the dominant reaction pathways for OH_{aq} formation may be attributed to the charge exchange reactions.

Acknowledgments

This work is funded and supported by the Air Force Office of Scientific Research (AFOSR Award No. FA9550-17-1-0257). The authors would like to thank Professor P. Thomas Vernier at the Frank Reidy Research Center for Bioelectrics, Old Dominion University, for his valuable advice and discussions on measurements of liquid phase OH.

ORCID iDs

Shutong Song  <https://orcid.org/0000-0003-1393-2790>
 Chunqi Jiang  <https://orcid.org/0000-0001-8895-2580>

- 1) H. Kajiyama, F. Utsumi, K. Nakamura, H. Tanaka, S. Toyokuni, M. Hori, and F. Kikkawa, *J. Clin. Biochem. Nutr.* **60**, 33 (2017).
- 2) C. Jiang, in *Bioelectrics*, ed. H. Akiyama and R. Heller (Springer Japan, Kumamoto, 2017) 1st ed., p. 337.

- 3) D. B. Graves, *Phys. Plasmas* **21**, 080901 (2014).
- 4) K. D. Weltmann, M. Polak, K. Masur, T. von Woedtke, J. Winter, and S. Reuter, *Contrib. Plasm. Phys.* **52**, 644 (2012).
- 5) S. Ikawa, K. Kitano, and S. Hamaguchi, *Plasma Processes Polym.* **7**, 33 (2010).
- 6) C. A. J. van Gils, S. Hofmann, B. K. H. L. Boekema, R. Brandenburg, and P. J. Bruggeman, *J. Phys. D: Appl. Phys.* **46**, 175203 (2013).
- 7) T. Kaneko, S. Sasaki, K. Takashima, and M. Kanzaki, *J. Clin. Biochem. Nutr.* **60**, 3 (2017).
- 8) D. B. Graves, *J. Phys. D: Appl. Phys.* **45**, 263001 (2012).
- 9) S. A. Norberg, W. Tian, E. Johnsen, and M. Kushner, *J. J. Phys. D: Appl. Phys.* **47**, 475203 (2014).
- 10) K. Ninomiya, T. Ishijima, M. Imamura, T. Yamahara, H. Enomoto, K. Takahashi, Y. Tanaka, Y. Uesugi, and N. Shimizu, *J. Phys. D: Appl. Phys.* **46**, 425401 (2013).
- 11) S. Sasaki, R. Honda, Y. Hokari, K. Takashima, M. Kanzaki, and T. Kaneko, *J. Phys. D: Appl. Phys.* **49**, 334002 (2016).
- 12) N. Kurake et al., *J. Phys. D: Appl. Phys.* **50**, 155202 (2017).
- 13) D. Ries, G. Dilecce, E. Robert, P. F. Ambrico, S. Dozias, and J. M. Pouvesle, *J. Phys. D: Appl. Phys.* **47**, 275401 (2014).
- 14) C. Q. Jiang and S. T. Song, *Jpn. J. Appl. Phys.* **56**, 046101 (2017).
- 15) S. Yonemori and R. Ono, *J. Phys. D: Appl. Phys.* **47**, 125401 (2014).
- 16) S. Kanazawa, H. Kawano, S. Watanabe, T. Furuki, S. Akamine, R. Ichiki, T. Ohkubo, M. Kocik, and J. Mizeraczyk, *Plasma Sources Sci. Technol.* **20**, 034010 (2011).
- 17) H. Tresp, M. U. Hammer, J. Winter, K. D. Weltmann, and S. Reuter, *J. Phys. D: Appl. Phys.* **46**, 435401 (2013).
- 18) T. Takamatsu, K. Uehara, Y. Sasaki, H. Miyahara, Y. Matsumura, A. Iwasawa, N. Ito, T. Azuma, M. Kohno, and A. Okino, *RSC Adv.* **4**, 39901 (2014).
- 19) H. Xu, C. Chen, D. X. Liu, D. H. Xu, Z. J. Liu, X. H. Wang, and M. G. Kong, *J. Phys. D: Appl. Phys.* **50**, 245201 (2017).
- 20) J. L. Walsh, J. J. Shi, and M. G. Kong, *Appl. Phys. Lett.* **88**, 171501 (2006).
- 21) Q. Xiong, X. P. Lu, K. Ostrikov, Y. Xian, C. Zou, Z. Xiong, and Y. Pan, *Phys. Plasmas* **17**, 043506 (2010).
- 22) H. M. Joh, J. Y. Choi, S. J. Kim, T. H. Kang, and T. H. Chung, *AIP Adv.* **7**, 085106 (2017).
- 23) X. Lu, G. V. Naidis, M. Laroussi, and K. Ostrikov, *Phys. Rep.* **540**, 123 (2014).
- 24) R. Ono, Y. Nakagawa, and T. Oda, *J. Phys. D: Appl. Phys.* **44**, 485201 (2011).
- 25) M. Sahni and B. R. Locke, *Ind. Eng. Chem. Res.* **45**, 5819 (2006).
- 26) G. Uchida, K. Takenaka, and Y. Setsuhara, *Jpn. J. Appl. Phys.* **55**, 01AH03 (2016).
- 27) Z. Liu, C. Zhou, D. Liu, D. Xu, W. Xia, Q. Cui, B. Wang, and G. M. Kong, *Phys. Plasmas* **25**, 013528 (2018).
- 28) E. B. Yan, J. K. Unthank, M. Castillo-Melendez, S. L. Miller, S. J. Langford, and D. W. Walker, *J. Appl. Physiol.* **98**, 2304 (2005).
- 29) L. X. Li, Y. Abe, Y. Nagasawa, R. Kudo, N. Usui, K. Imai, T. Mashino, M. Mochizuki, and N. Miyata, *Biomed. Chromatogr.* **18**, 470 (2004).
- 30) M. Saran and K. H. Summer, *Free Radic. Res.* **31**, 429 (1999).
- 31) T. J. Mason, J. P. Lorimer, D. M. Bates, and Y. Zhao, *Ultrason. Sonochem.* **1**, S91 (1994).
- 32) D. X. Liu, P. Bruggeman, F. Iza, M. Z. Rong, and M. G. Kong, *Plasma Sources Sci. Technol.* **19**, 025018 (2010).
- 33) P. Bruggeman and D. C. Schram, *Plasma Sources Sci. Technol.* **19**, 045025 (2010).